

## Modelling strain hardening during cyclic thermal shock tests of tungsten

Aleksandr Zinovev<sup>1</sup>, Laurent Delannay<sup>2</sup>, Dmitry Terentyev<sup>1</sup>

<sup>1</sup>*Institute for Nuclear Materials Science, SCK CEN, Boeretang 200, B-2400 Mol, Belgium*

<sup>2</sup>*iMMC, Université catholique de Louvain, Av. Georges Lemaître 4, B-1348 Louvain-la-Neuve, Belgium*

**Abstract:** An original model is proposed in order to simulate elastic-plastic transients inside tungsten subjected to cyclic thermal loads expected due to plasma instabilities called “edge-localized modes” in ITER. The model assumes that plasticity is achieved by thermally-activated dislocation motion and it accounts for both isotropic and kinematic hardening. Their relative contributions to the material response are tuned in order to reproduce uniaxial tensile tests performed at different temperatures and different strain rates in various tungsten grades. The model is designed for application as a user-defined material law in fully implicit finite element simulation of thermomechanical loads. The first predictions of the build-up of residual stresses are observed to be qualitatively in line with experimental trends.

*Keywords:* fusion, thermal fatigue, residual stresses, kinematic hardening

### 1 Introduction

One of the main challenges in the development of the ITER fusion device [1] is the qualification of pre-selected grades of reliable in-vessel materials. Due to its high melting point, good thermal conductivity, low erosion rate and other advantages [2], tungsten (W) has been selected as the plasma-facing material for the divertor monoblocks in the vacuum vessel of ITER, which will withstand heavy thermal loads during operation. Periodical plasma instabilities called “edge-localised modes” (ELM) are expected to deposit about 1–10 GW m<sup>-2</sup> of thermal energy onto the divertor surface within ~0.2–0.5 ms short pulses occurring at a frequency of ~1 Hz [3]. This may cause thermomechanical fatigue and cracking of plasma-facing components (PFC). The violation of structural integrity of PFCs is an operational safety issue, as it can lead to the coolant ingress into the vessel and consequent termination of fusion reaction.

So far, experimental characterization of W as material for PFCs involved mechanical [4–8], high heat flux [9,10], thermal shock [11] and neutron irradiation testing [12,13]. The effects of ELM on the material response were investigated by exposing the surface of various W grades to a pulsed scanning electron beam [3,14] or pulses of plasma in devices such as quasi-stationary plasma accelerator (QSPA) [15,16], linear devices Pilot-PSI [17] or Magnum-PSI [18] (accompanied by laser pulses) mimicking the heat loads expected in the ITER divertor region. The occurrence of plasticity was demonstrated by transmission electron microscopy (TEM) observations even after exposure to power density below the threshold of surface damage [19]. With the increase of the pulse number, the dislocations, initially formed at grain boundaries (GBs), evolved into tangles and pile-ups, which can be regarded as microscopic precursors of fatigue damage. Surface roughening was reported already at a low deposited power density and number of cycles [20–22]. The reduction of the sample base temperature, which raises the yield stress, did not affect the roughness but induced surface cracks [21] under certain conditions. According to Ref. [23], in a wrought W sample with base temperature of 800 °C, microcracks appeared at the applied thermal power density above 0.15 GW m<sup>-2</sup>, whereas following exposure below that threshold only increased surface roughness was observed. Microcracks were formed in a process initiated by plastic deformation at high temperature [20,24]. Macrocracks were reported to appear at power density above 0.70 GW m<sup>-2</sup>. Such macrocracks are likely to be due to the

brittleness of W [23]. Indeed, in the cooling phase of the cycle, large tensile thermal stresses arise between the hot exposed area and the cold surrounding material [20].

Residual stresses after thermal shocks were measured in several works [15,16]. The value of residual stress usually quickly reached a maximum, several hundred MPa, after a few thermal pulses. Depending on the base temperature, it remained nearly unchanged for ~100–300 thermal shocks and, in the case of higher base temperature equal to 650 °C, decreased down to ~50 MPa after ~150–300 thermal shocks. The significant reduction of residual stresses can be explained by recrystallization of the subsurface region, as well as its melting and resolidification [15]. The increase of the base temperature usually led to a more rapid decrease of residual tensile stresses with the number of thermal pulses, resulting in a lower amplitude of residual stress. The development of a fatigue crack network was also found to relax the stresses developed during the thermal shock experiments [15].

Finite element method (FEM) can be useful in order to simulate the evolution of residual stresses in the subsurface region of material exposed to ELM-like pulses. Thermal fatigue of W-based PFCs is determined by the presence of weak spots at which micro cracks are initiated. However, so far, attempts to simulate W components subjected to high heat load or thermal shocks, usually relied on highly simplified constitutive laws, such as perfect plasticity [25,26]. There is hardening in the W grades and it involves both isotropic and kinematic components. The Bauschinger effect, which is well known e.g. in steels [27], has however scarcely been studied in W. Fatigue tests of different W grades did confirm early plasticity upon load reversal [28]. Whereas isotropic hardening results from the increasing dislocation density due to mutual pinning, kinematic hardening in single-phase materials occurs owing to dislocation pile-ups at GBs. In W exposed to cyclic heat loads, the pile ups thus raise microscopic stresses at locations of intergranular cracks nucleation [29,30]. In a previous study, kinematic hardening law was considered in order to estimate the fatigue life of a W block exposed to large thermal load, without a thorough investigation of the effect of backstresses [31]. One difficulty is that the strain hardening response deduced from uniaxial tensile tests does not cover the wide range of temperature (up to 2000–3000 °C [31]) and strain rate (up to  $8 \text{ s}^{-1}$  [32]), attained at the plasma-facing surface during the combined action of stationary heat loads and ELMs.

In the present work, simulations rely on a physically-based modelling of the temperature- and rate-sensitivity of the plastic response of two specific commercial W grades. This allows properly accounting for the continuously evolving temperature and strain rate during the heat loads. The first grade is a hammered bar fabricated by Plansee AG (Austria) which is compliant with the ITER specifications, and referred to as “IGP” (which stands for “ITER-grade Plansee”). The second one is the same material after recrystallization at 1600 °C for 1 h [3–5], and referred to as “RX”. Although the divertor monoblocks will be fabricated from wrought W, recrystallized W is of interest too because a thin subsurface volume of the monoblocks will gradually recrystallize during operation due to high temperature on the surface, affecting its mechanical properties [33].

Whereas previous assessment of the constitutive law involved only a monotonically increasing load under uniaxial tension [4,34,35], the model is here adapted to account, in an original manner, for the kinematic hardening affecting elastic-plastic transients during cyclic loading in a representative volume element (RVE) of a macroscopic block of W.

The outline of the paper is as follows. After the introduction, in Section 2, we describe the experiments which inspired us to develop and apply the model of plasticity with kinematic hardening. Its mathematical formulation as well as the principle of the optimisation algorithm are briefly provided in Section 3. The model parameterization with the help of tensile test simulations, and the results of thermal shock test simulations are presented and discussed in Sections 4 and 5 correspondingly, while

conclusions are drawn in Section 6. Appendix A provides complementary information about the numerical implementation of the model.

## 2 Motivating experiments

The response measured during uniaxial tensile tests was used to parameterize the plasticity model. Experimental data reported in [3] is complemented with mechanical tests performed at Belgian Nuclear Research Centre SCK CEN in the range 300–600 °C and  $6 \cdot 10^{-5}$ – $6 \cdot 10^{-3}$  s<sup>-1</sup> [4,5]. The hammered grade was tested in the longitudinal orientation, in which the elongated grains are parallel to the load direction, hence the postfix “L” in the “IGP-L” tag.

Cyclic response could only be deduced from fatigue tests of a different W grade (whose density is, however, below the ITER specification [36]) reported by Habainy et al. [28]. This grade is referred to as “Habainy” in the text and figures. The corresponding stress-strain loops presented in Fig. 1 were obtained at 480 °C and they involve three strain amplitudes. The amplitude of the backstress in these tests can be estimated at 225–275 MPa, if it is approximated as one half of the difference between the maximum stress in the loops (~450 MPa) and the stress at which plasticity occurs upon unloading (~-100–0 MPa).

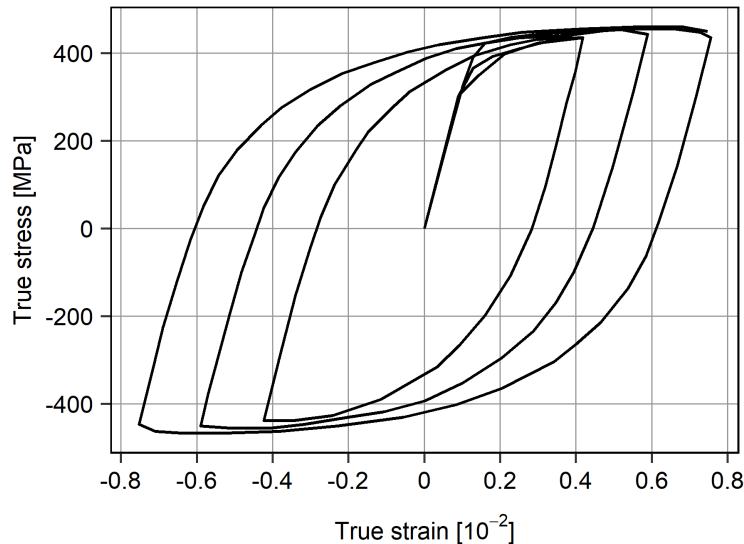


**Fig. 1.** Stress-strain loops obtained in Ref. [28] revealing kinematic hardening in low cycle fatigue tests of forged W at 500 °C. The strain amplitudes are 0.42%, 0.58% and 0.75%. The W grade is different from IGP and is referred to as “Habainy”.

The model was also applied to the simulation of a series of thermal shock tests performed by Wirtz et al. in the electron-beam facility JUDITH 1 on IGP W in the longitudinal (“L”) or transverse (“T”) orientation as well as on RX W [3]. The samples in the experiments were fixed to a heated stage to maintain constant base temperature on one side (27 °C, 400 °C or 1000 °C) whereas the opposite side was exposed to pulses of an electron beam that mimicked ELMs in ITER (depositing 190 MW m<sup>-2</sup> or 380 MW m<sup>-2</sup> of thermal power in 1 ms pulses). The surface temperature was reported to increase by 350 °C and 700 °C in every pulse at respectively the two values of thermal power density. Various patterns of surface damage were reported as a result of the exposure.

### 3 Model description

The proposed model relies on a fully implicit time integration of  $J_2$  elasto-plasticity theory which has been adapted in order to account, on the one hand, for kinematic hardening and, on the other hand, for strain rate sensitivity resulting from thermally activated dislocation glide.

The deviatoric part of the Cauchy stress tensor  $\boldsymbol{\sigma}$  is denoted  $\mathbf{s}$ . Stress heterogeneity at the microscopic scale gives rise to a backstress  $\mathbf{X} = \mathbf{s} - \boldsymbol{\beta}$ , where  $\boldsymbol{\beta}$  represents the deviatoric stress acting on mobile dislocations. The latter backstress evolves with plastic strain according to:

$$\dot{\mathbf{X}} = A\dot{\boldsymbol{\epsilon}}^p - B\mathbf{X}\dot{p} - C\mathbf{X} \exp(-H_0/k_B T) \quad \text{Eq. 1}$$

where dots represent time derivatives whereas  $A$  and  $B$  are two scalar parameters which are typical of saturating kinematic hardening laws [37–39]. The variable  $\dot{\boldsymbol{\epsilon}}^p$  is the tensor of plastic strain rate and  $\dot{p} = \sqrt{\frac{2}{3}} \|\dot{\boldsymbol{\epsilon}}^p\|$  is the rate of increase of the accumulated plastic strain. The last term on the right-hand side causes the backstress to relax even in the absence of plasticity:  $C$  is a fixed material parameter,  $H_0$  is an activation energy,  $k_B$  is the Boltzmann constant and  $T$  is the temperature.

In crystals with body-centred cubic lattice (BCC), dislocation motion is impeded when the resolved shear stress is lower than a threshold value called the athermal stress  $\sigma_{ath}$ . According to the von Mises criterion, viscoplastic yielding then occurs on the condition that:

$$\sigma_{eq} = \sqrt{\frac{3}{2} \boldsymbol{\beta} : \boldsymbol{\beta}} > \sigma_{ath} = \sigma_{y0} + \alpha \mu b \sqrt{\rho} \quad \text{Eq. 2}$$

In this expression,  $\sigma_{y0}$  accounts for the lattice friction and the contribution to yield stress due to the Hall-Petch effect,  $\alpha$  is a dimensionless scalar parameter,  $\mu$  is the elastic shear modulus,  $b$  is the norm of the Burgers vector and  $\rho$  is the local dislocation density which increases in the course of deformation, causing isotropic strain hardening.

The plastic strain rate is a function of the overstress ratio  $\xi = (\sigma_{eq} - \sigma_{ath})/\hat{\sigma}$ , in which  $\hat{\sigma}$  is a fixed parameter defining the level of the effective stress above which dislocation glide is hindered by viscous drag. When  $\xi > 1$ , the plastic strain rate is computed as  $\dot{p} = \xi \dot{p}_0$  where

$$\dot{p}_0 = \dot{p}_0 \left( 1 - \exp\left(-\frac{ab}{k_B T} (\sigma_{eq} - \sigma_{ath})\right) \right) \quad \text{Eq. 3}$$

In this Arrhenius-type relationship,  $a$  is the area swept by a dislocation jump. At lower stress levels, i.e. when  $\xi < 1$ , dislocation slip is thermally activated and the plastic strain rate is expressed as [40–42]:

$$\dot{p} = \dot{p}_0 \exp\left(-\frac{\Delta G}{k_B T}\right) = \dot{p}_0 \exp\left(-\frac{F_0}{k_B T} (1 - \xi^r)^q\right) \quad \text{Eq. 4}$$

where  $\Delta G$  is the free enthalpy required for a mobile dislocation to overcome short-range obstacles [43], the exponents  $q = 1.4$  and  $r = 0.5$  as well as the reference activation energy  $F_0$  are fixed [44].

The evolution of the dislocation density involves a competition between storage and recovery mechanisms, which is modelled following Kocks and Mecking [45,46]:

$$\dot{\rho} = k_1 \left( \sqrt{\rho} - \frac{\rho}{\sqrt{\rho_{sat}}} \right) \dot{p} \quad \text{with} \quad \rho_{sat} = \left( \xi \frac{k_1}{k_2} \right)^2 \quad \text{Eq. 5}$$

The saturating value of the dislocation density  $\rho_{sat}$  thus evolves with the overstress factor  $\xi$ . This implies that  $\rho_{sat}$  depends on both the strain rate and the temperature. Indeed, recovery mechanisms are thermally activated. As a consequence, the modelled stress response is both temperature- and rate- dependent through Eq. 2. The parameters  $k_1$  and  $k_2$  have constant values.

The constitutive law is integrated fully implicitly relying on a Newton-Raphson iterative scheme. The radial return mapping algorithms allow integrating  $J_2$  plasticity with a single scalar equation. The development of a backstress imposes solving a set of six equations in which the unknowns are the five linearly independent components of  $\boldsymbol{\beta}$  and the increment of accumulated plastic strain  $\Delta p = \dot{p}\Delta t$ . Mathematical developments described in the appendix show how the procedure proposed in [47] can be adapted from  $J_2$  plasticity to the present temperature-dependent, viscoplastic model. This procedure also provides a consistent tangent operator that is useful for instance when the model is used as the user-defined material law of an implicit finite element solver. The detailed description of the numerical implementation is provided in the appendix. The model can be applied either as a user-defined material law UMAT of the commercial FEM solver Abaqus, or in a stand-alone procedure.

In order to simulate thermal shocks, the model was parameterized with the help of an iterative optimization algorithm. The parameter optimization started from an initial guess and then converged to produce the best fit of all the considered tensile tests of a given grade with a single set of parameters. The objective function was the total sum of squares of differences between the simulated ( $\sigma_s^{i,n}$ ) and the experimental ( $\sigma_e^{i,n}$ ) true stress values at three reference points (0.02%, 0.2% and 0.5% of plastic strain) as illustrated in Fig. 2 for the  $n^{\text{th}}$  stress-strain curve. The fitting has been performed in a narrow strain range, as the thermal strain achieved in a single cycle was expected not to exceed 1% as demonstrated by macroscopic FEM simulation of thermal shocks in [48] and in the present work below. The hardening rate at 1% of plastic strain was also monitored to match experimental values.

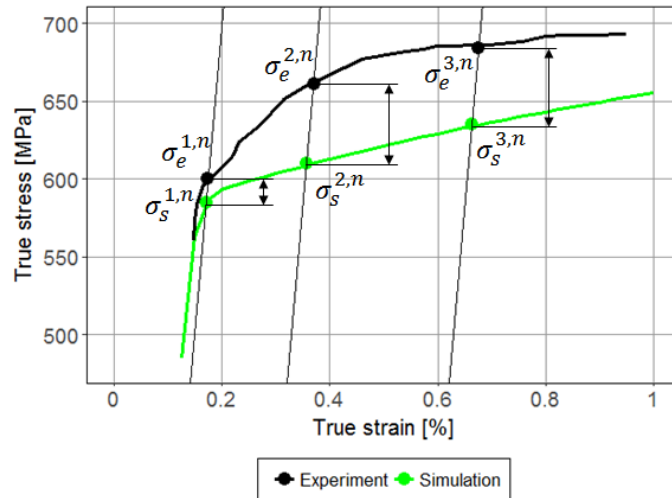


Fig. 2. Illustration of the evaluation of the objective function. The squares of differences between experimental and simulated values of stress were summed up.

## 4 Results

### 4.1 Simulation of uniaxial tensile tests

Fig. 3 compares the fitted (lines) and experimental (symbols) stress-strain curves at various constant temperatures and strain rates. Certain curves are lowered by 150 MPa or 100 MPa to avoid excessive overlapping, as noted in the legend. Notice that the rate sensitivity decreases with the increase of

temperature, since the contribution of the thermal stress component decreases. Some of the model parameters were considered to have a priori known values before launching the iterative search algorithm: the Young modulus  $E = 388$  GPa, Poisson ratio  $\nu = 0.28$ , Burgers vector  $b = 0.274$  nm and initial dislocation density  $\rho_0 = 4 \cdot 10^{12} \text{ m}^{-2}$  and  $9 \cdot 10^{10} \text{ m}^{-2}$  for IGP-L and RX W correspondingly [49]. The elastic properties were assumed to be independent on temperature in this work, because the available experimental data do not allow us to assess this influence. Table 1 lists the fitted material parameters. The only difference in the parameter sets for the two W grades is the initial dislocation density.

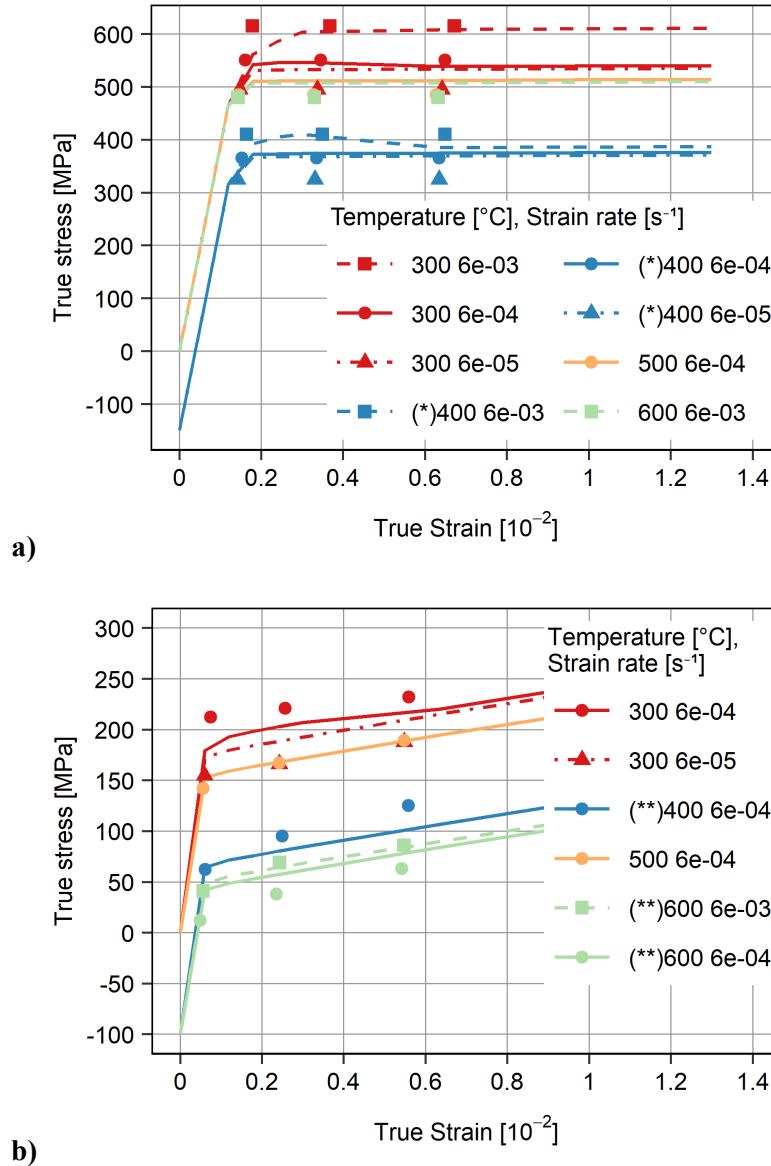


Fig. 3. The best fit of the model (lines) to experimental stress-strain data (symbols) in the experimentally-explored range of temperatures: (a) for IGP-L W and (b) RX W. Curves marked with (\*) or (\*\*) are shifted downwards by 150 MPa or by 100 MPa correspondingly to improve readability.

Table 1. Model parameters independent on the W grade.

Parameter	$E$	$\nu$	$A$	$B$	$\sigma_{y0}$	$F_0$	$\alpha$
Value	388	0.28	48000	300	30	0.31	5

Unit	GPa	-	MPa	-	MPa	(in $\mu b^3$ )	-
Parameter	$a$	$\dot{p}_0$	$\hat{\sigma}$	$C$	$H_0$	$k_1$	$k_2$
Value	365	$10^{12}$	250	$1.6 \cdot 10^4$	0.457	$8.3 \cdot 10^7$	40
Unit	(in $b^2$ )	$s^{-1}$	MPa	$s^{-1}$	eV	$m^{-1}$	-

The same model was used to simulate the strain-controlled fatigue tests performed at 480 °C in [28]. The dislocation density was not reported in the cited paper. The best fit of the experimental data was obtained with a value  $\rho_0 = 6.4 \cdot 10^{11} m^{-2}$  whereas the two parameters of the Kocks-Mecking hardening law also needed adjustment:  $k_1 = 8 \cdot 10^7 m^{-1}$  and  $k_2 = 100$ . The simulated curves are compared with the reported experimental results in Fig. 4.

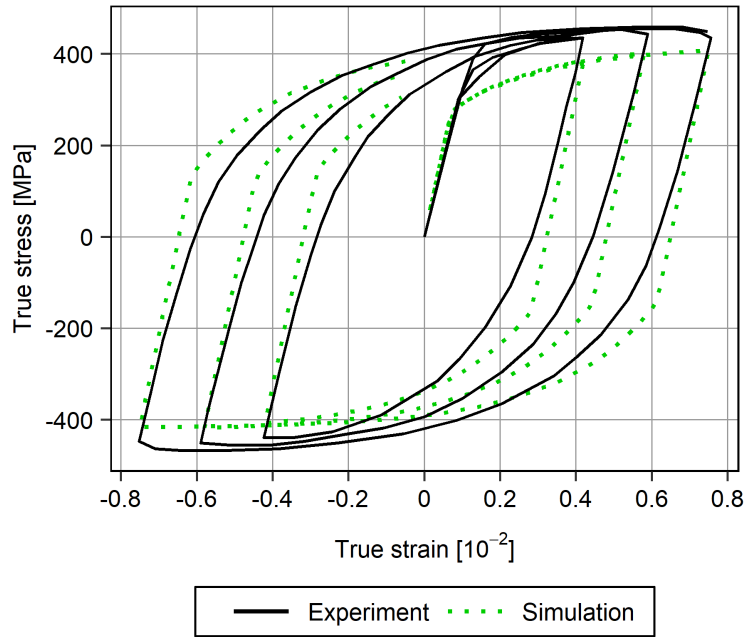


Fig. 4. Simulated fatigue tests and comparison to the experiment of the forged W from Ref. [28].

#### 4.2 Simulation of internal stresses due to thermal shocks

FEM was used to predict the distribution of temperature, strain and internal stresses during a thermal pulse acting on a macroscopic block made of W. The new material law was used to compute the response of W. The mesh shown in Fig. 5(a-c) represents one quarter of the experimental sample  $12 \times 12 \times 5 mm^3$  investigated in Ref. [3]. The base temperature was 400 °C. The central square of  $4 \times 4 mm^2$  on the top surface was exposed to a varying thermal flux whereas the bottom surface was kept at constant temperature. The heat capacity of W was set equal to  $145 J kg^{-1} K^{-1}$ , the conductivity was set equal to  $135 W m^{-1} K^{-1}$  and the thermal expansion coefficient was chosen equal to  $5 \cdot 10^{-6} K^{-1}$ , as respective means of reported values in the whole considered temperature range 25–1700 °C [25,50,51].

Fig. 5(a-b) shows the distribution of strain components in the W block at the highest temperature when the heat load is  $380 MW m^{-2}$ . LE33 and LE11 denote, respectively, the out-of-plane ( $z$  direction) and the in-plane ( $x$  direction or  $y$  direction) normal logarithmic strains. The equivalent plastic strain in the centre of the heated area does not exceed 1% and the strain mode is nearly uniaxial in this region of interest with regard to damage development. This justifies the use of simplified simulations of thermal shocks using the stand-alone mode and assuming uniform temperature and uniaxial straining.

Fig. 5c demonstrates the temperature distribution at the end of the thermal pulse (in kelvins). The temperature evolution at the centre of the heated area is shown in Fig. 6 for different power densities and base temperatures. The temperature rises by 350 °C or 700 °C at 190 MW m<sup>-2</sup> or 380 MW m<sup>-2</sup> correspondingly (in accordance with the values reported in [3]), reaching the maximum at the end of the heating phase (1 ms after the onset of heating). Then, the most significant temperature drop is observed in the next millisecond after switching off the thermal pulse. This allows using a symmetric triangular temperature profile in the simplified simulations described below.

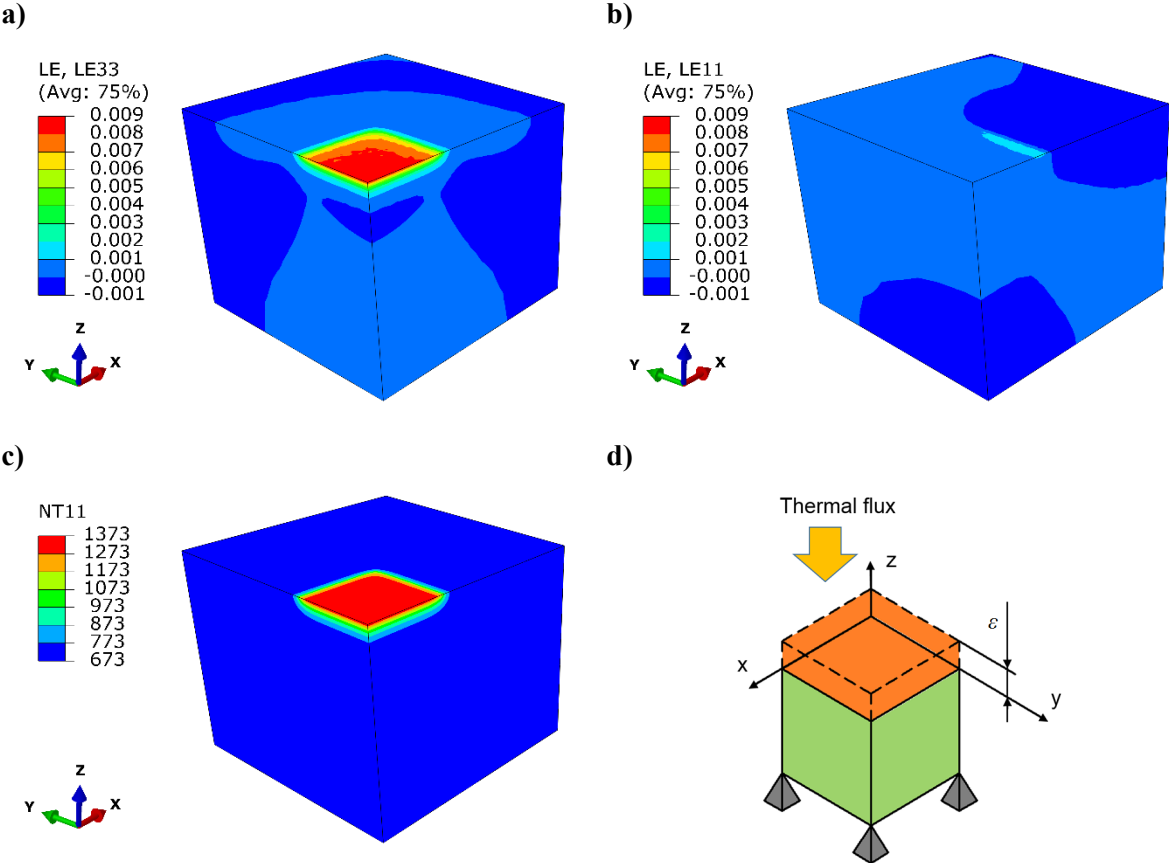


**Fig. 5. (a-c) The mesh used in FEM analysis of thermal shock and distribution of (a) the normal strain component in the direction  $z$  LE33 (out-of-plane), (b) the normal strain component in the direction  $x$  LE11 (in-plane), (c) temperature (in kelvins) at the end of a heat pulse at base temperature 400 °C and the power density 380 MW m<sup>-2</sup>. The heated area 4x4 mm<sup>2</sup> is clearly seen. (d) Schematic view of the simulation box used in the stand-alone calculations in the initial and deformed state (orange colour) with  $\epsilon$  showing the out-of-plane thermal strain.**

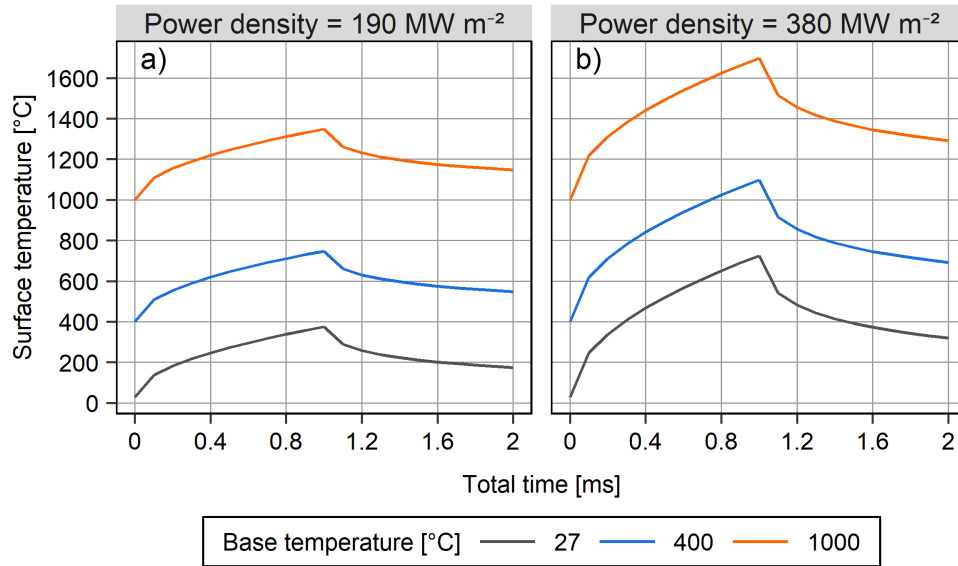


Fig. 6. Evolution of temperature in the heated surface of a W block exposed to thermal shocks, depending on their power density and the base temperature. (a) at  $190 \text{ MW m}^{-2}$ , (b) at  $380 \text{ MW m}^{-2}$ .

In the simplified stand-alone simulations the computational cell was constrained in directions  $x$  and  $y$ , and was free to deform along direction  $z$ , allowing thermal expansion, as schematically shown in Fig. 5d.

Fig. 7 compares the prediction of the simplified stand-alone simulation to the FEM prediction in the centre of the heated area. The in-plane ( $E_{11}$ ) and out-of-plane ( $E_{33}$ ) normal strain components are considered. The difference is small enough to justify saving computational time when aiming to obtain qualitative description of the mechanical response of W to thermal shocks. The stand-alone simulation slightly overestimates the out-of-plane strain peak, thus providing a conservative estimate.

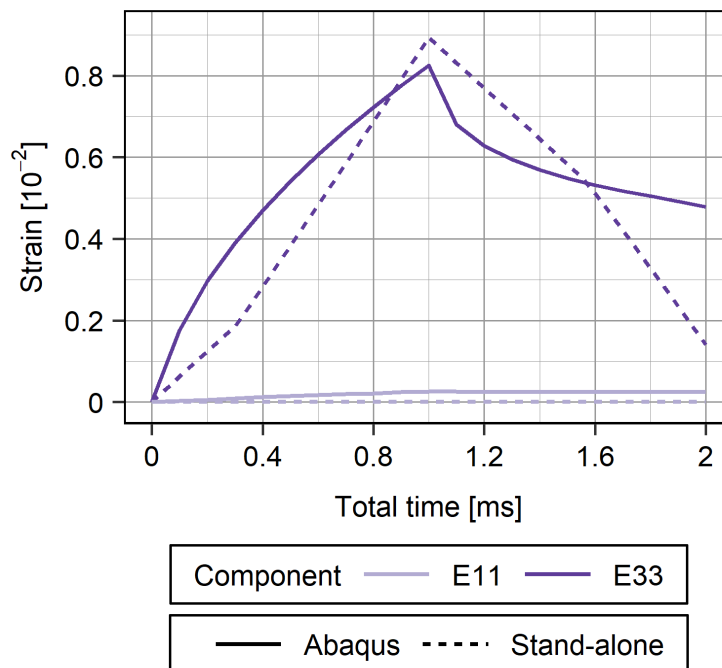
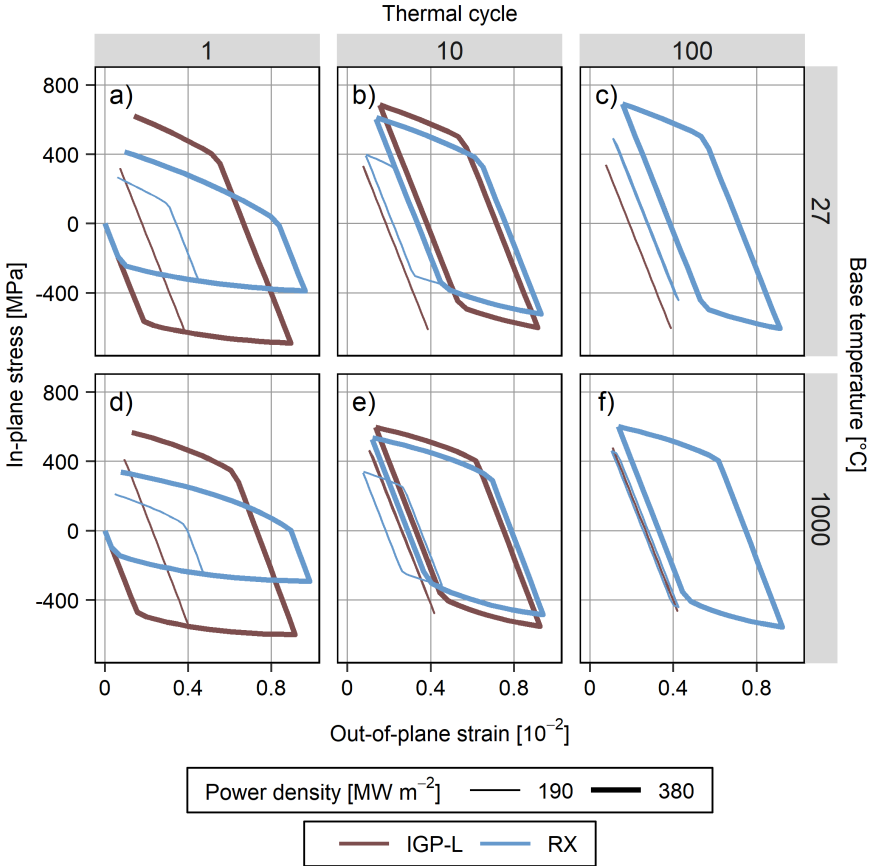


Fig. 7. Strain components recorded in the FEM simulations and the stand-alone simulations at  $400 \text{ °C}$  base temperature and  $380 \text{ MW m}^{-2}$  power density.

A series of simplified simulations of cyclic thermal shocks were performed aiming to determine the influence of the base temperature and the power density on the development of internal stresses. The three W grades (“IGP-L”, “RX” and “Habainy”) were considered under the conditions of the thermal shock experiments of Wirtz et al. [3], i.e. three base temperatures (27 °C, 400 °C, 1000 °C) and two levels of power density (190 MW m<sup>-2</sup> and 380 MW m<sup>-2</sup>). One hundred thermal pulses were simulated and the values of the thermally-induced in-plane stress and out-of-plane strain were recorded. A selection of the predicted stress-strain loops are shown in Fig. 8. The evolution of the maximal tensile stress as a function of the number of cycles is shown in Fig. 9. It is assumed to characterise the severity of residual stresses in the component, providing an indication of the number of thermal cycles prior to the formation of microcracks.



**Fig. 8. Mechanical response of the three W grades to thermal shocks of different power density in terms of the in-plane stress vs. the out-of-plane strain. (a), (b) and (c) at 27 °C, (d), (e) and (f) at 1000 °C. (a) and (d) show the 1<sup>st</sup> cycle, (b) and (e) show the 10<sup>th</sup> cycle, (c) and (f) show the 100<sup>th</sup> cycle.**

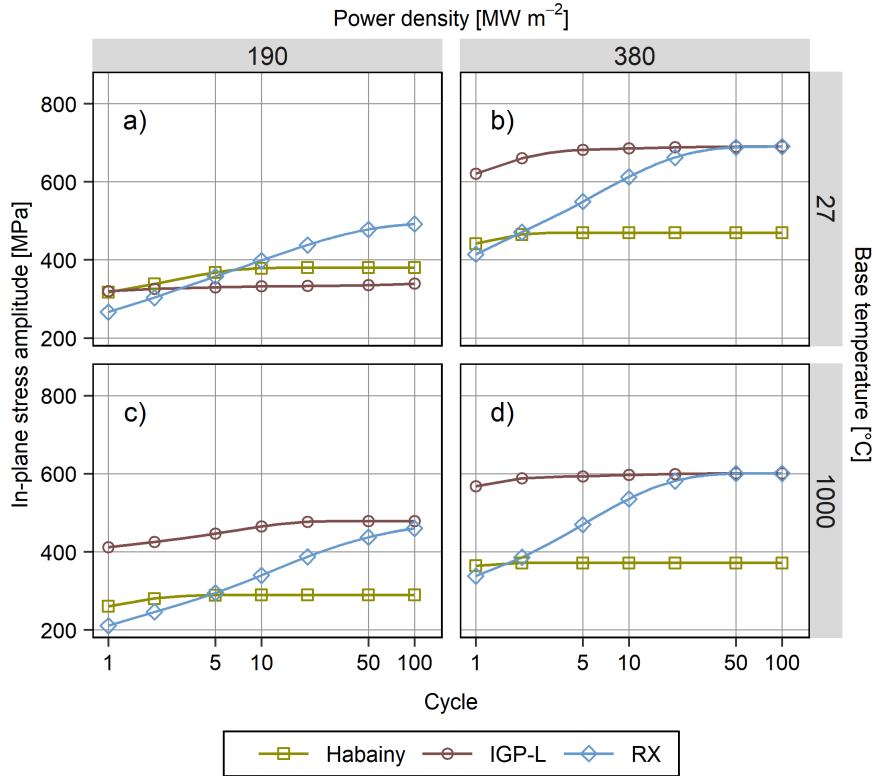


Fig. 9. The evolution of the in-plane tensile stress amplitude obtained in the simulations of thermal shocks for three studied W grades. (a) and (c) at 190 MW m<sup>-2</sup>, (b) and (d) at 380 MW m<sup>-2</sup>. (a) and (b) at 27 °C, (c) and (d) at 1000 °C.

## 5 Discussion

One of the assumptions of the present work is that the kinematic hardening, for which there is evidence at 480 °C in the cyclic tests performed by Habainy [28], might still be present at much higher temperatures. Certainly, accounting for such kinematic hardening in the present work has contributed to improve the ability of the proposed model to reproduce, with a single set of parameters, the uniaxial tensile tests performed in a wide range of temperature (300–600 °C) and at different strain rates ( $6 \cdot 10^{-5}$ – $6 \cdot 10^{-3}$  s<sup>-1</sup>). Whether the observed hardening still has a kinematic nature at such high temperatures can only be confirmed by cyclic testing, which is for now unavailable. It must be born in mind that the backstress amplitude actually measures the heterogeneity of stresses witnessed, respectively, by the mobile dislocations accommodating plasticity and by dislocations already piled up against GBs. It is a repulsive stress which tends to separate the two types of dislocations. During monotonic loading, mobile dislocations progress against the backstress (“they have wind in the face”) since the backstress makes it more difficult to reach and pile up at the GBs. On the opposite, already immobilized dislocations are pushed against the GBs and this increases the stress at the head of pile-up which becomes denser. Hence, the stress amplitude in the vicinity of GBs, where damage (i.e. microvoid nucleation) is expected to initiate, is larger than the stress level probed macroscopically under monotonic loading. On the other hand, isotropic hardening, more than kinematic hardening, leads to a progressive increase of the maximum stress attained during cyclic loading.

In this work, the influence of dynamic recrystallization in W on strength and internal stresses was not really considered. The proposed model assumes that the grain size remains constant and that the dislocation density reduces only as a result of thermally activated recovery mechanisms. The model

predictions are likely to be more accurate at temperatures sufficiently low to avoid recrystallization. This probably is the case at some depth inside PFC of the fusion divertor where the amplitude of cyclic stresses is most likely to cause the formation of fatigue cracks. Besides, the strain gradients at a depth are expected to be lower than at the surface (due to a limited depth of propagation of heat from short transients). Thus, even though contribution to hardening resulting from the accumulation of geometrically necessary dislocations (GNDs) is possible, we disregard it in the model. In the same time, the expected temperature is not low enough to reveal the asymmetry of the tension-compression response of W. Further update of the model might benefit from consideration of the asymmetry effect, requiring development of a reliable experimental database, which is scarce currently.

An advantage of the proposed hardening model is that it accounts for the fact that both strain hardening and rate sensitivity continuously evolve as a result of temperature variations during the cyclic thermal shocks. The model may also be used while switching off such influence of temperature on the mechanical response of W. Fig. 10 compares the outcome of simulations performed with high power density ( $380 \text{ MW m}^{-2}$ ) at base temperature  $27 \text{ }^\circ\text{C}$ , with and without sensitivity of the model parameters. Fig. 10a shows the stress-strain loops predicted after 10 cycles in IGP-L material. The evolution of the maximum tensile stress as a function of the number of cycles is presented in Fig. 10b for the three materials. Simulations in which the plasticity model parameters were insensitive to temperature excursions are labelled with the “no T” tag. The difference in stress between the pairs of corresponding simulations can reach 100 MPa.

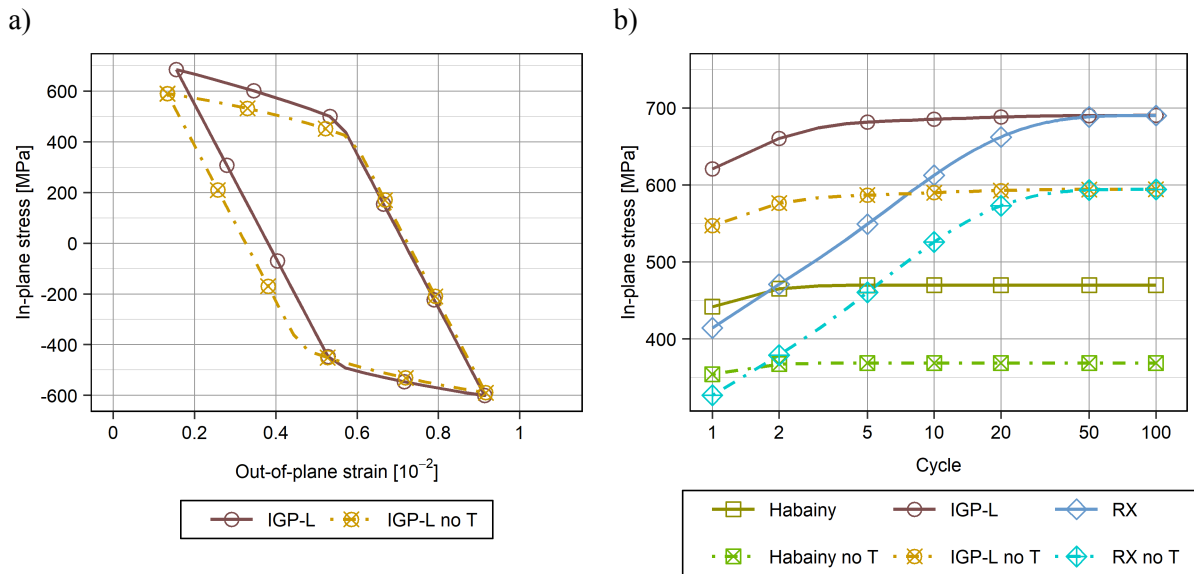


**Fig. 10.** Illustration of the temperature effect on the plasticity model parameters in a thermal shock simulation with power density  $380 \text{ MW m}^{-2}$  and base temperature  $27 \text{ }^\circ\text{C}$ . The “no T” tag indicates that the temperature effect was disabled. (a) An example of stress-strain loops observed in IGP-L W. (b) Evolution of the maximal tensile stress in three materials.

The stress-strain loops summarised in Fig. 8 reveal that there was little plastic deformation in the first thermal cycle when applying the low power density,  $190 \text{ MW m}^{-2}$  (solid lines), to both IGP-L and RX W. Then, there was a gradual degeneration of the loops and the material ended up in the state of elastic shakedown. The IGP-L W reached this state sooner than the RX W (already at the 10<sup>th</sup> cycle). This may be due to the higher initial yield stress, observed in tensile tests. The absence of plastic deformation in the elastic shakedown state greatly increases the material lifetime in fatigue conditions. This can explain why no damage was observed on the surface of IGP-L W. On the contrary, RX W exposed to

190 MW m<sup>-2</sup> in [3] attained higher plastic deformation before reaching the state of elastic shakedown, which, probably, explains the surface roughness observed in the experiment.

When the high power density was applied, 380 MW m<sup>-2</sup> (dashed lines), there was significant plastic deformation and the stress-strain loops did not degenerate in all three materials. The mean strain value and the strain amplitude increased by a factor 2–3 as compared to the lower power density simulations. The loops for IGP-L and RX W fully overlapped after 100 cycles. Larger plastic deformation in every cycle can explain the development of damage and cracks on the surface of W blocks exposed to high power density in the experiment.

In addition, our analysis showed that the presence of the initial ELM-induced plastic deformation (attained in the first cycle) did not allow the material to return to its initial deformation-free state at the end of the heat pulse. The post-heated area maintained some bulging after cooling down. Such surface roughening, which is regularly observed experimentally already after a few pulses, is a well known precursor of crack nucleation at later stages of ELM exposure.

According to Fig. 9, the stress amplitude decreases with the increase of base temperature for the three materials exposed to 380 MW m<sup>-2</sup>. Hence, the materials should sustain a larger number of thermal pulses at high base temperature and the density of surface microcracks should be lower after any given number of pulses, which agrees with experiments.

The cited thermal shock experiments [3] brought the following evidence: the IGP W samples exposed to 100 pulses of power density 190 MW m<sup>-2</sup>, showed no surface modifications in the whole tested range of temperatures, except for the sample with the “T” orientation, in which small cracks formed at base temperature of 27 °C. Cracks were found in all the samples exposed to high power density (380 MW m<sup>-2</sup>), while the number and size of cracks decreased with the increase of base temperature. The roughness of the heated surface of RX W increased even at low power density of thermal shocks and above room temperature.

## 6 Conclusions

A novel isotropic viscoplastic model was used in order to simulate the stress state in W exposed to cyclic thermal shock loads mimicking the plasma instability, ELM, anticipated in ITER. The proposed model relies on a simplified but physically-sound representation of the strain rate sensitivity resulting from thermally-activated dislocation glide and it also accounts for kinematic hardening. Using a single set of parameters, the model produced valid predictions of the mechanical response of three W grades under uniaxial tension at different temperatures and strain rates. It can be used as a stand-alone computer code or as a user-defined material subroutine in an implicit finite element solver.

A qualitative agreement with the thermal shock experiments has been obtained:

- i) Elastic deformation dominated in IGP-L W exposed to low power density of 190 MW m<sup>-2</sup>, which may explain little to no surface modification in the corresponding experiment.
- ii) Plastic deformation dominated in IGP-L W exposed to high power density of 380 MW m<sup>-2</sup> and recrystallized W under both exposure conditions, which may explain the formation of surface cracks in the experiment.
- iii) Stress amplitude during cyclic heat loads increased faster in the recrystallized W, due to its larger work hardening capacity, indicating a higher probability of crack formation.

- iv) The stress amplitude decreased with the increase of the base temperature, which may explain why reducing the base temperature lowered the density of surface microcracks in the experiment.
- v) The systematic prediction of plasticity in the first ELM-cycles could be at the origin of surface roughness, a precursor of crack nucleation at later stages of ELM exposure.

### Acknowledgments

This work has been carried out within the framework of the EUROfusion Consortium and has received funding from the Euratom research and training programme 2014–2018 and 2019–2020 under grant agreement No. 633053. The views and opinions expressed herein do not necessarily reflect those of the European Commission. LD is mandated by the FNRS.

### Appendix A. Mathematical formulation of the plasticity model

Fully implicit time integration of the viscoplastic material law with kinematic hardening follows a numerically efficient procedure inspired from the solution which is described in [47] in the case of rate insensitive  $J_2$  plasticity.

At every iteration of the FE simulation, the routine computing the material response receives from the finite element solver the Cauchy stress  $\boldsymbol{\sigma}|_t$  and the backstress  $\mathbf{X}|_t$ , which have both been rotated to ensure objectivity, as well as the dislocation density  $\rho|_t$  computed at the end of the previous time step. The solver obviously also provides the temperature, the strain increment  $\Delta\boldsymbol{\varepsilon}$  and the time increment  $\Delta t$ .

The elastic predictor is first computed from the deviatoric part  $\Delta\mathbf{e}$  of the strain increment:  $\mathbf{s}^{tr} = \mathbf{s}|_t + 2\mu \Delta\mathbf{e}$ . The corresponding effective stress acting on mobile dislocations is computed as  $\boldsymbol{\beta}^{tr} = \mathbf{s}^{tr} - \mathbf{X}|_t$  and the strain increment is considered purely elastic on the condition that:

$$\sqrt{\frac{3}{2} \boldsymbol{\beta}^{tr} : \boldsymbol{\beta}^{tr}} \leq \sigma_{y0} + \alpha\mu b\sqrt{\rho|_t} \quad \text{Eq. A 1}$$

In case an elastic response, the deviatoric part of Cauchy stress is updated while accounting for the thermally-activated relaxation of the backstress (Eq. 2):

$$\mathbf{s}|_{t+\Delta t} = \boldsymbol{\beta}^{tr} + \check{\mathbf{X}} \quad \text{where} \quad \check{\mathbf{X}} = \mathbf{X}|_t \exp(-C\Delta t) \quad \text{Eq. A 2}$$

On the other hand, if the deformation increment is viscoplastic, then the following yield criterion must be fulfilled:

$$f(\boldsymbol{\beta}, \dot{p}, \rho) = \sqrt{\frac{3}{2} \boldsymbol{\beta} : \boldsymbol{\beta}} - (\sigma_{y0} + \alpha\mu b\sqrt{\rho}) - \xi \hat{\sigma} \leq 0 \quad \text{Eq. A 3}$$

The overstress factor  $\xi$  is a function of the plastic strain rate  $\dot{p}$  and the temperature  $T$ . When dislocation slip is thermally activated ( $0 < \xi \leq 1$ ), the expression of  $\xi$  derives from Eq. 4

$$\xi = \left( 1 - \left( \frac{k_B T}{F_0} \ln \left( \frac{\dot{\rho}}{\dot{\rho}_0} \right) \right)^{1/q} \right)^{1/r}, \quad \text{Eq. A 4}$$

whereas at larger applied stresses it reduces to  $\xi = \dot{\rho} / \dot{\rho}_0 > 1$  meaning that dislocation slip is slowed down by viscous drag.

If plasticity occurs during the current time step, a fully implicit integration of Eq. 5 causes the dislocation density to evolve as follows:

$$\sqrt{\rho} = \xi \frac{k_1}{k_2} + \left( \sqrt{\rho}|_t - \xi \frac{k_1}{k_2} \right) \exp \left( -\frac{k_2}{2\xi} \Delta p \right) \quad \text{where} \quad \Delta p = \dot{p} \Delta t \quad \text{Eq. A 5}$$

The backstress is updated according to a fully implicit integration of Eq. 1 which, after introducing  $\tilde{\mathbf{A}} = \mathbf{A} \exp(-C \Delta t)$ , leads to:

$$\mathbf{k}(\boldsymbol{\beta}, \Delta p) = \mathbf{s}^{tr} - 2\mu \mathbf{N} \Delta p - \left( \boldsymbol{\beta} + \frac{\tilde{\mathbf{X}} + \tilde{\mathbf{A}} \mathbf{N} \Delta p}{1 + B \Delta p} \right) = \mathbf{0} \quad \text{Eq. A 6}$$

Together with  $f(\boldsymbol{\beta}, \dot{p}, \rho) = 0$ , the latter tensor equation forms a set of six linearly independent scalar equations which must be solved iteratively. It turns out (see [47] for details in case of rate independent plasticity) that, when adopting a Newton-Raphson scheme, there is an explicit expression of the iterative corrections to the plastic strain increment  $\Delta p$  and to the  $\boldsymbol{\beta}$  tensor:

$$\delta \Delta p = \left( f - \frac{df}{d\sigma_{eq}} \mathbf{N} : \mathbf{k} \right) / \left( \frac{df}{dp} + \frac{df}{d\sigma_{eq}} \left( \frac{1.5\tilde{\mathbf{A}} - B \mathbf{N} : \tilde{\mathbf{X}}}{(1 + B \Delta p)^2} \right) \right) \quad \text{Eq. A 7}$$

$$\delta \boldsymbol{\beta} = \frac{1}{1 + 1.5 c_1} (-\mathbf{k} + c_2 \tilde{\mathbf{X}} + c_3 \mathbf{N}) - \left( 2\mu + \frac{\tilde{\mathbf{A}}}{(1 + B \Delta p)^2} \right) \delta \Delta p \mathbf{N} \quad \text{Eq. A 8}$$

with:

$$c_1 = \left( 2\mu + \frac{\tilde{\mathbf{A}}}{1 + B \Delta p} \right) \frac{\Delta p}{\sigma_{eq}}, \quad c_2 = \frac{B}{(1 + B \Delta p)^2} \delta \Delta p, \quad c_3 = c_1 (c_2 \mathbf{N} : \tilde{\mathbf{X}} - \mathbf{N} : \mathbf{k}) \quad \text{Eq. A 9}$$

$$\frac{df}{d\sigma_{eq}} = 1 + \left( \alpha \mu b \frac{d\sqrt{\rho}}{d\xi} - \hat{\sigma} \right) \frac{d\xi}{d\dot{\rho}_0} \frac{d\dot{\rho}_0}{d\sigma_{eq}} \quad \text{Eq. A 10}$$

$$\frac{df}{dp} = \alpha \mu b \frac{d\sqrt{\rho}}{dp} \quad \text{Eq. A 11}$$

## References

- [1] ITER - the way to new energy, (n.d.). <https://www.iter.org/> (accessed December 14, 2020).
- [2] J. Linke, T. Loewenhoff, V. Massaut, G. Pintsuk, G. Ritz, M. Rödiger, A. Schmidt, C. Thomser, I. Uytendhouwen, V. Vasechko, M. Wirtz, Performance of different tungsten grades under transient thermal loads, *Nucl. Fusion*. 51 (2011) 073017. <https://doi.org/10.1088/0029-5515/51/7/073017>.
- [3] M. Wirtz, J. Linke, T. Loewenhoff, G. Pintsuk, I. Uytendhouwen, Thermal shock tests to qualify different tungsten grades as plasma facing material, *Phys. Scr.* T167 (2016) 014015. <https://doi.org/10.1088/0031-8949/T167/1/014015>.
- [4] A. Zinovev, D. Terentyev, A. Dubinko, L. Delannay, Constitutive law for thermally-activated plasticity of recrystallized tungsten, *J. Nucl. Mater.* 496 (2017) 325–332. <https://doi.org/10.1016/j.jnucmat.2017.09.044>.

- [5] C. Yin, D. Terentyev, T. Pardoën, A. Bakaeva, R.H. Petrov, S. Antusch, M. Rieth, M. Vilémová, J. Matějčiček, T. Zhang, Tensile properties of baseline and advanced tungsten grades for fusion applications, *Int. J. Refract. Met. Hard Mater.* 75 (2018) 153–162. <https://doi.org/10.1016/j.ijrmhm.2018.04.003>.
- [6] D. Terentyev, J. Riesch, S. Lebediev, T. Khvan, A. Zinovev, M. Rasiński, A. Dubinko, J.W. Coenen, Plastic deformation of recrystallized tungsten-potassium wires: Constitutive deformation law in the temperature range 22–600 °C, *Int. J. Refract. Met. Hard Mater.* 73 (2018) 38–45. <https://doi.org/10.1016/j.ijrmhm.2018.01.012>.
- [7] W. Guan, S. Nogami, M. Fukuda, A. Hasegawa, Tensile and fatigue properties of potassium doped and rhenium containing tungsten rods for fusion reactor applications, *Fusion Eng. Des.* 109–111 (2016) 1538–1542. <https://doi.org/10.1016/j.fusengdes.2015.11.030>.
- [8] E. Gaganidze, D. Rupp, J. Aktaa, Fracture behaviour of polycrystalline tungsten, *J. Nucl. Mater.* 446 (2014) 240–245. <https://doi.org/10.1016/j.jnucmat.2013.11.001>.
- [9] T. Hirai, F. Escourbiac, V.R. Barabash, A. Durocher, A. Fedosov, L. Ferrand, T. Jokinen, V. Komarov, M. Merola, S. Carpentier-Chouchana, N. Arhipov, V. Kuznetsov, A. Volodin, S. Suzuki, K. Ezato, Y. Seki, B. Riccardi, M. Bednarek, P. Gavila, Status of technology R&D for the ITER tungsten divertor monoblock, *J. Nucl. Mater.* 463 (2015) 1248–1251. <https://doi.org/10.1016/j.jnucmat.2014.12.027>.
- [10] S. Panayotis, T. Hirai, V.R. Barabash, A. Durocher, F. Escourbiac, J. Linke, T. Loewenhoff, M. Merola, G. Pintsuk, I. Uytendhouwen, M. Wirtz, Self-castellation of tungsten monoblock under high heat flux loading and impact of material properties, *Nucl. Mater. Energy.* 12 (2017) 200–204. <https://doi.org/10.1016/j.nme.2016.10.025>.
- [11] W. Van Renterghem, I. Uytendhouwen, Effect of thermal heat loads on the microstructure of recrystallized double forged tungsten, *Fusion Eng. Des.* 88 (2013) 1650–1654. <https://doi.org/10.1016/j.fusengdes.2013.05.011>.
- [12] V.R. Barabash, G. Federici, M. Rödiger, L.L. Snead, C.H. Wu, Neutron irradiation effects on plasma facing materials, *J. Nucl. Mater.* 283–287 (2000) 138–146. [https://doi.org/10.1016/S0022-3115\(00\)00203-8](https://doi.org/10.1016/S0022-3115(00)00203-8).
- [13] A. Hasegawa, M. Fukuda, T. Tanno, S. Nogami, Neutron Irradiation Behavior of Tungsten, *Mater. Trans.* 54 (2013) 466–471. <https://doi.org/10.2320/matertrans.MG201208>.
- [14] R. Zalavutdinov, A. Novokhatsky, V. Gusev, V. Bukhovets, A. Gorodetsky, V. Kuznetsov, N. Litunovsky, A. Makhankov, I. Mazul, E. Mukhin, Y. Petrov, T. Rybkina, N. Sakharov, S. Tolstyakov, A. Voronin, A. Zakharov, Electron beam treatment of tungsten mock-ups, *Phys. Scr.* T170 (2017) 014043. <https://doi.org/10.1088/1402-4896/aa8b00>.
- [15] V.A. Makhlij, I.E. Garkusha, S. V. Malykhin, A.T. Pugachov, I. Landman, J. Linke, S. Pestchanyi, V. V. Chebotarev, V.I. Tereshin, Residual stresses in tungsten under exposures with ITER ELM-like plasma loads, *Phys. Scr.* T138 (2009) 014060. <https://doi.org/10.1088/0031-8949/2009/T138/014060>.
- [16] V.A. Makhlij, I.E. Garkusha, N.N. Aksenov, B. Bazylev, I. Landman, J. Linke, S. V. Malykhin, A.T. Pugachov, M.J. Sadowski, E. Skladnik-Sadowska, M. Wirtz, Tungsten damage and melt losses under plasma accelerator exposure with ITER ELM relevant conditions, *Phys. Scr.* T159 (2014) 014024. <https://doi.org/10.1088/0031-8949/2014/T159/014024>.
- [17] T.W. Morgan, J.J. Zielinski, B.J. Hensen, H.Y. Xu, L. Marot, G. De Temmerman, Reduced damage threshold for tungsten using combined steady state and transient sources, *J. Nucl. Mater.* 438 (2013) 784–787. <https://doi.org/10.1016/j.jnucmat.2013.01.168>.
- [18] G.G. van Eden, T.W. Morgan, H.J. van der Meiden, J. Matejicek, T. Chraska, M. Wirtz, G. De Temmerman, The effect of high-flux H plasma exposure with simultaneous transient heat loads on tungsten surface damage and power handling, *Nucl. Fusion.* 54 (2014) 123010. <https://doi.org/10.1088/0029-5515/54/12/123010>.
- [19] W. Van Renterghem, I. Uytendhouwen, T. Loewenhoff, M. Wirtz, TEM analysis of recrystallized double forged tungsten after exposure in JUDITH 1 and JUDITH 2, *Nucl. Mater. Energy.* 9 (2016) 484–489. <https://doi.org/10.1016/j.nme.2016.04.003>.
- [20] I. Uytendhouwen, M. Decréton, T. Hirai, J. Linke, G. Pintsuk, G. Van Oost, Influence of recrystallization on thermal shock resistance of various tungsten grades, *J. Nucl. Mater.* 363–365 (2007) 1099–1103. <https://doi.org/10.1016/j.jnucmat.2007.01.146>.
- [21] A. Huber, A.S. Arakcheev, G. Sergienko, I. Steudel, M. Wirtz, A. V. Burdakov, J.W. Coenen, A. Kreter, J. Linke, P. Mertens, V. Philipps, G. Pintsuk, M. Reinhart, U. Samm, A.A. Shoshin, B. Schweer, B. Unterberg, M. Zlobinski, Investigation of the impact of transient heat loads applied by laser irradiation on ITER-grade tungsten, *Phys. Scr.* T159 (2014) 014005. <https://doi.org/10.1088/0031-8949/2014/T159/014005>.

- [22] T. Loewenhoff, S. Antusch, G. Pintsuk, M. Rieth, M. Wirtz, High pulse number thermal shock testing of tungsten alloys produced by powder injection molding, *Nucl. Mater. Energy.* 20 (2019) 100680. <https://doi.org/10.1016/j.nme.2019.100680>.
- [23] T. Hirai, G. Pintsuk, J. Linke, M. Batilliot, Cracking failure study of ITER-reference tungsten grade under single pulse thermal shock loads at elevated temperatures, *J. Nucl. Mater.* 390–391 (2009) 751–754. <https://doi.org/10.1016/j.jnucmat.2009.01.313>.
- [24] S. Pestchanyi, I.E. Garkusha, I. Landman, Simulation of tungsten armour cracking due to small ELMs in ITER, *Fusion Eng. Des.* 85 (2010) 1697–1701. <https://doi.org/10.1016/j.fusengdes.2010.05.005>.
- [25] M. Li, E. Werner, J.-H. You, Cracking behavior of tungsten armor under ELM-like thermal shock loads: A computational study, *Nucl. Mater. Energy.* 2 (2015) 1–11. <https://doi.org/10.1016/j.nme.2014.10.001>.
- [26] M. Li, J.-H. You, Interpretation of the deep cracking phenomenon of tungsten monoblock targets observed in high-heat-flux fatigue tests at 20 MW/m<sup>2</sup>, *Fusion Eng. Des.* 101 (2015) 1–8. <https://doi.org/10.1016/j.fusengdes.2015.09.008>.
- [27] S.D. Antolovich, R.W. Armstrong, Plastic strain localization in metals: origins and consequences, *Prog. Mater. Sci.* 59 (2014) 1–160. <https://doi.org/10.1016/j.pmatsci.2013.06.001>.
- [28] J. Habainy, S. Iyengar, Y. Lee, Y. Dai, Fatigue behavior of rolled and forged tungsten at 25°, 280° and 480 °C, *J. Nucl. Mater.* 465 (2015) 438–447. <https://doi.org/10.1016/j.jnucmat.2015.06.032>.
- [29] A. Dubinko, D. Terentyev, A. Bakaeva, K. Verbeken, M. Wirtz, M. Hernández-Mayoral, Evolution of plastic deformation in heavily deformed and recrystallized tungsten of ITER specification studied by TEM, *Int. J. Refract. Met. Hard Mater.* 66 (2017) 105–115. <https://doi.org/http://dx.doi.org/10.1016/j.ijrmhm.2017.03.004>.
- [30] Y. Ueda, K. Schmid, M. Balden, J.W. Coenen, T. Loewenhoff, A. Ito, A. Hasegawa, C. Hardie, M. Porton, M.R. Gilbert, Baseline high heat flux and plasma facing materials for fusion, *Nucl. Fusion.* 57 (2017) 092006. <https://doi.org/10.1088/1741-4326/aa6b60>.
- [31] J. Du, Y. Yuan, M. Wirtz, J. Linke, W. Liu, H. Greuner, FEM study of recrystallized tungsten under ELM-like heat loads, *J. Nucl. Mater.* 463 (2015) 219–222. <https://doi.org/10.1016/j.jnucmat.2014.10.044>.
- [32] I. Uytendhouwen, Degradation of first wall materials under ITER relevant loading conditions, Universiteit Gent, 2011.
- [33] G. Pintsuk, M. Bednarek, P. Gavila, S. Gerzoskovitz, J. Linke, P. Lorenzetto, B. Riccardi, F. Escourbiac, Characterization of ITER tungsten qualification mock-ups exposed to high cyclic thermal loads, *Fusion Eng. Des.* 98–99 (2015) 1384–1388. <https://doi.org/10.1016/j.fusengdes.2015.01.037>.
- [34] D. Terentyev, X. Xiao, A. Dubinko, A. Bakaeva, H. Duan, Dislocation-mediated strain hardening in tungsten: Thermo-mechanical plasticity theory and experimental validation, *J. Mech. Phys. Solids.* 85 (2015) 1–15. <https://doi.org/10.1016/j.jmps.2015.08.015>.
- [35] H. Sheng, G. Van Oost, E.E. Zhurkin, D. Terentyev, V.I. Dubinko, I. Uytendhouwen, J. Vleugels, High temperature strain hardening behavior in double forged and potassium doped tungsten, *J. Nucl. Mater.* 444 (2014) 214–219. <https://doi.org/10.1016/j.jnucmat.2013.09.057>.
- [36] T. Hirai, S. Panayotis, V.R. Barabash, C. Amzallag, F. Escourbiac, A. Durocher, M. Merola, J. Linke, T. Loewenhoff, G. Pintsuk, M. Wirtz, I. Uytendhouwen, Use of tungsten material for the ITER divertor, *Nucl. Mater. Energy.* 9 (2016) 616–622. <https://doi.org/10.1016/j.nme.2016.07.003>.
- [37] P.J. Armstrong, C.O. Frederick, A Mathematical Representation of the Multi Axial Bauschinger Effect. CEGB Report RD/B/N 731, 1966. [https://www.scirp.org/\(S\(czeh2tfqyw2orz553k1w0r45\)\)/reference/ReferencesPapers.aspx?ReferenceID=1260344](https://www.scirp.org/(S(czeh2tfqyw2orz553k1w0r45))/reference/ReferencesPapers.aspx?ReferenceID=1260344).
- [38] C.O. Frederick, P.J. Armstrong, A mathematical representation of the multiaxial Bauschinger effect, *Mater. High Temp.* 24 (2007) 1–26. <https://doi.org/10.3184/096034007X207589>.
- [39] J. Lemaitre, J.L. Chaboche, *Mechanics of Solid Materials*, Cambridge University Press, 1990.
- [40] U.F. Kocks, A.S. Argon, M.F. Ashby, *Thermodynamics and kinetics of slip*, 1975.
- [41] H.J. Frost, M.F. Ashby, *Deformation mechanism maps: the plasticity and creep of metals and ceramics*, 1982.
- [42] G. Lemoine, L. Delannay, H. Idrissi, M.-S. Colla, T. Pardoën, Dislocation and back stress dominated viscoplasticity in freestanding sub-micron Pd films, *Acta Mater.* 111 (2016) 10–21. <https://doi.org/10.1016/j.actamat.2016.03.038>.
- [43] P.S. Follansbee, U.F. Kocks, A constitutive description of the deformation of copper based on the use of the mechanical threshold stress as an internal state variable, *Acta Metall.* 36 (1988) 81–93.

- [https://doi.org/10.1016/0001-6160\(88\)90030-2](https://doi.org/10.1016/0001-6160(88)90030-2).
- [44] K. Ono, Temperature Dependence of Dispersed Barrier Hardening, *J. Appl. Phys.* 39 (1968) 1803–1806. <https://doi.org/10.1063/1.1656434>.
- [45] H. Mecking, U.F. Kocks, Kinetics of flow and strain-hardening, *Acta Metall.* 29 (1981) 1865–1875. [https://doi.org/10.1016/0001-6160\(81\)90112-7](https://doi.org/10.1016/0001-6160(81)90112-7).
- [46] Y. Estrin, H. Mecking, A unified phenomenological description of work hardening and creep based on one-parameter models, *Acta Metall.* 32 (1984) 57–70. [https://doi.org/10.1016/0001-6160\(84\)90202-5](https://doi.org/10.1016/0001-6160(84)90202-5).
- [47] I. Doghri, *Mechanics of Deformable Solids*, Springer Berlin Heidelberg, Berlin, Heidelberg, 2000. <https://doi.org/10.1007/978-3-662-04168-0>.
- [48] A. Zinovev, D. Terentyev, L. Delannay, Finite element analysis of heat load of tungsten relevant to ITER conditions, *Phys. Scr. T170* (2017) 014002. <https://doi.org/10.1088/0031-8949/2017/T170/014002>.
- [49] A. Dubinko, *Plastic Deformation of Tungsten under Fusion-Plasma Exposure Conditions*, Universiteit Gent, 2018.
- [50] J.-H. You, I. Komarova, Probabilistic failure analysis of a water-cooled tungsten divertor: Impact of embrittlement, *J. Nucl. Mater.* 375 (2008) 283–289. <https://doi.org/10.1016/j.jnucmat.2008.01.009>.
- [51] M. Li, E. Werner, J.-H. You, Fracture mechanical analysis of tungsten armor failure of a water-cooled divertor target, *Fusion Eng. Des.* 89 (2014) 2716–2725. <https://doi.org/10.1016/j.fusengdes.2014.07.011>.